



HAL
open science

Micromechanical Investigation of the Hydromechanical Behaviors of Carbonates Contribution of In-Situ Strain Field Measurement By Means of SEM And Optic Digital Image Correlation

Jérémie Dautriat, Michel Bornert, Nicolas Gland, Alexandre Dimanov, Jean Raphanel, Olga Vizika

► To cite this version:

Jérémie Dautriat, Michel Bornert, Nicolas Gland, Alexandre Dimanov, Jean Raphanel, et al.. Micromechanical Investigation of the Hydromechanical Behaviors of Carbonates Contribution of In-Situ Strain Field Measurement By Means of SEM And Optic Digital Image Correlation. *Petrophysics – The SPWLA Journal of Formation Evaluation and Reservoir Description*, 2010, 51 (6), pp.388-398. hal-00625650

HAL Id: hal-00625650

<https://hal.science/hal-00625650v1>

Submitted on 3 Sep 2021

HAL is a multi-disciplinary open access archive for the deposit and dissemination of scientific research documents, whether they are published or not. The documents may come from teaching and research institutions in France or abroad, or from public or private research centers.

L'archive ouverte pluridisciplinaire **HAL**, est destinée au dépôt et à la diffusion de documents scientifiques de niveau recherche, publiés ou non, émanant des établissements d'enseignement et de recherche français ou étrangers, des laboratoires publics ou privés.



Distributed under a Creative Commons Attribution 4.0 International License

MICROMECHANICAL INVESTIGATION OF THE HYDROMECHANICAL BEHAVIOURS OF CARBONATES CONTRIBUTION OF IN-SITU STRAIN FIELD MEASUREMENT BY MEANS OF SEM AND OPTIC DIGITAL IMAGE CORRELATION

J. Dautriat^(1,2), M. Bornert⁽²⁾, N. Gland⁽¹⁾, A. Dimanov⁽²⁾, J. Raphanel⁽²⁾, O. Vizika⁽¹⁾

⁽¹⁾ Institut Français du Pétrole, 1&4 av. de Bois-Préau, 92852 Rueil-Malmaison, France

⁽²⁾ Laboratoire de Mécanique des Solides, Ecole Polytechnique, 91128 Palaiseau, France

ABSTRACT

In a previous study (Dautriat, 2008), we have studied the macroscopic hydro-mechanical behaviour of a moderately heterogeneous carbonate reservoir analogue, undergoing triaxial testing along several proportional stress paths, ranging from hydrostatic compression to axial compression. Evolutions of permeabilities and compressibilities during loading have been measured and correlated and the yield envelope has been determined. Structural heterogeneities have been shown to strongly affect the initiation of brittle and plastic damages. There is a trend to interpret the macroscopic response in term of micro-mechanisms without actual observation and identification. While post-mortem characterisation techniques (HPMI, SEM and CTRX/ μ -CTRX images) inform qualitatively on the damage mechanisms activated at the grain and aggregate scales, a quantitative and continuous micro-mechanical investigation is needed to follow the history of the deformation and the localisation during compression. We have therefore performed in-situ observations during loading at different scales. First, small samples have been deformed by simple compression inside a SEM, in order to identify the physical deformation and damage micro-mechanisms responsible for the evolutions of the transport properties. Then, larger samples have been subjected to axial compression in an hydraulic press and have been observed by optical methods, in order to better understand the complex interactions governing the macroscopic behaviour. Observations of the micro-mechanisms during mechanical tests are difficult for geomaterials because the levels of deformation are low (below the percent), but feasible with some care and appropriate recording devices; different regions of small parallelepipedic samples have been imaged using different magnifications to focus either on grain or contact, or to visualise the aggregates. Direct optical observations on bigger cylindrical samples, mechanically loaded on conventional UCS testing machines, have also been performed at two different scales by means of high resolution digital cameras. On one side, the full sample is imaged ($\sim 20\mu\text{m}$ resolution) in order to characterise the overall response. On the opposite spot side, a centimetric area has been considered ($\sim 3\mu\text{m}$ resolution), at which scale the composite nature of the rock made of microporous and dense calcite grains is revealed. Those two scales imaging experiments have been combined with efficient Digital Image Correlation (DIC) post-treatments, able to detect very small displacements and evolutions of the microstructures (strain accuracy better than 10^{-3}). The comparisons of SEM images taken stepwise, reveal deformations hardly detectable by conventional

observations, such as: opening or closure of pre-existing microcracks, nucleation of new microcracks and relative movements at grain interfaces. Different strain accommodation regimes are also observed in dense and microporous grains, respectively brittle and diffuse. The movies at sample scale show that the heterogeneity of strain is correlated to the local distribution of the aggregates, which confirms the post-mortem observations.

INTRODUCTION

The method of local displacement measurement and strain field computation by correlation of digital images acquired at different steps of a mechanical test (either continuous or incremental), is a powerful tool for the characterization the mechanical behaviour of heterogeneous materials (Chu, 1985, Bruck, 1989). Surprisingly, it has been too rarely applied to geomaterials (Lenoir 2007, Vales, 2008), which present however strong localisations in relation to their generally heterogeneous microstructure. We have applied this technique on carbonate samples of Estailades, deformed through simple compression tests. From the hydromechanical measurements and the post mortem observations by HPMI, SEM and MCT, it has been shown how the microstructural heterogeneities of this carbonate are linked to the activated damage mechanisms, which influence the directional permeabilities and the compressibilities evolutions (Dautriat, 2009, Yale, 1998). The DIC extensometry by field measurement highlights the role of these heterogeneities on the evolution of the strain field, and particularly on the localisation and the damage mechanisms. To our knowledge, this technique has never been applied to this kind of heterogeneous carbonate. First, a set-up of two optical cameras was used to measure the evolution of strain field at macroscopic and mesoscopic scales on flat truncated surfaces of large cylindrical samples. Then, an experimental in-situ compression inside the chamber of an Environmental Scanning Electron Microscope has been used to measure strain field (Doumalin, 1999) at microscopic scale on the side of small parallelipipedic samples. For SCAL and geomechanical studies, 2D/3D DIC might offer a way to explore more precisely the origins of the macroscopic evolution of the hydromechanical properties by investigating the deformation field at different scales. Identifying the deformation mechanisms activated locally and understanding how multiscales heterogeneities affect and govern the behaviour, serve correct interpretation and give basis to develop behaviour models.

MICROSTRUCTURAL/PETROPHYSICAL CHARACTERIZATION

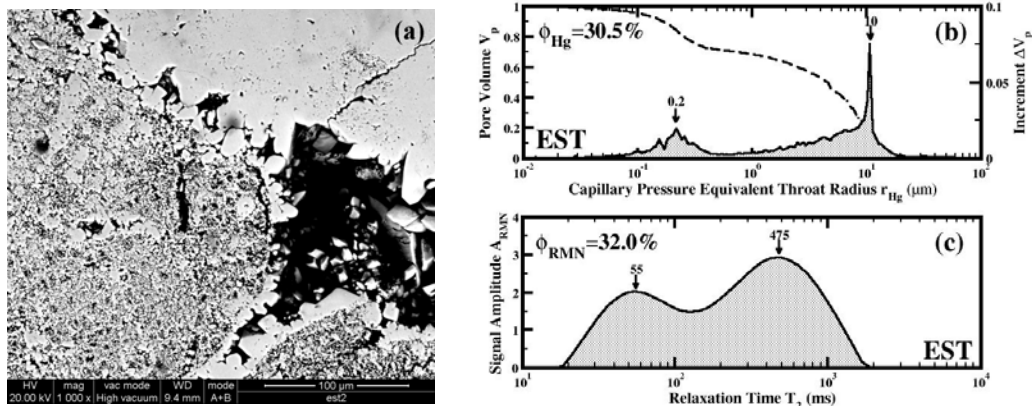


Figure 1: (a) SEM image (BSE) of Estailades carbonate; triple junction: microporous (left) and dense (top) aggregates and macropore (right); (b) Hg porosimetry showing a bimodal distribution of pore throat radii; (c) NMR T2 distribution showing a bimodal distribution.

The Estailades Limestone is a moderately porous and permeable carbonate of granular microstructure, composed almost exclusively of calcite (99%) grains (between 1 μ m to 10 μ m) and forming two kinds of aggregates, either highly dense or microporous (see Fig.1(a)), of size ranging from 100 μ m to 500 μ m. The porosity is bimodal (as shown by NMR T2 distribution in Fig.1(c)) with a large mesoporosity (inter-aggregates) and a smaller microporosity (intra-aggregates) having pore throats radii of 10 μ m and 0.2 μ m, respectively (HPMI in Fig. 1(b)). At the macroscopic scale of a plug, this carbonate presents some degree of heterogeneity, inferred from porosity and permeability data. Indeed, the average porosity, determined by dry and saturated weights, is 28%, but it varies from one plug to another from 24% up to 31% because of the heterogeneous distribution of the different aggregates. The average permeability measured on full-length (Dautriat, 2009) is 125mD, but it varies as well accordingly from 50 to 150mD.

CARBONATE HYDROMECHANICAL PROPERTIES (@ K=0)

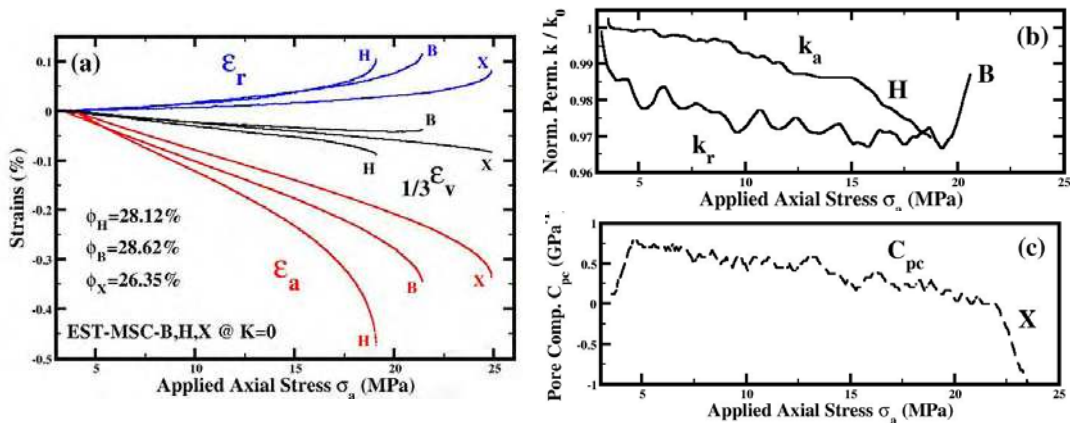


Figure 2: (a) Stress-strains curves of three Estailades (H, B and X) samples in saturated, drained conditions for simple compression tests; axial, radial, and volumic strains are respectively of red, blue and black colors; (b) Evolution of axial and radial permeabilities and (c) pore compressibility of the three Estailades samples.

We recall through Figure 2 a brief hydro-mechanical characterization of the Estailades Limestone in drained condition, under triaxial loading with stress path parameter $K=0$ (simple compression at 3MPa confinement) and small loading rates (0.1MPa/min). The stress path parameter K is defined as $\Delta\sigma_r/\Delta\sigma_a$, the ratio between the radial and axial stress increases. A more complete characterization (K ranging from 0 to 1) can be found in Dautriat (2008, 2009). Triaxial experiments were performed in drained conditions at constant pore pressure of 1 MPa along the $K=0$ stress path on three Estailades samples of porosity ranging from 26.3% to 28.6%. In average, we observe that the less porous samples, exhibit higher strength and higher Young Modulus. The Young modulus ranges from 5GPa to 6GPa, for a constant Poisson ratio of 0.25 and the saturated strength ranges from 19MPa to 25MPa. Nevertheless, local microstructural heterogeneities in a sample may affect the mechanical behaviour and strength/moduli fluctuations can still be observed. Different volumic strain evolutions can also be observed depending on the heterogeneity; some samples exhibit dilatancy and permeability increase before peak stress and failure while others remains purely compactant up to brittle failure. Additionally, we have performed simple compression tests, in dry condition, on two others different samples. The Unconfined Compressive Strengths respectively of 14 MPa and 16 MPa were smaller owing to unconfined condition. Meanwhile, the static Young moduli respectively of 8GPa and 9GPa were

larger, since wet condition is known to alter the mechanical behaviour of rocks in relation to their mineralogy. In the following work, all tests are performed at $K=0$ (without confinement), in dry conditions, with higher loading rates.

DIGITAL IMAGE CORRELATION METHOD

Extensometry by means of field measurement, based on Digital Image Correlation (DIC), is an ‘optical’ measurement method, without displacement sensor or contact gauge. It consists in comparing an image acquired at a reference undeformed state to images acquired at different steps of deformation during a mechanical test. More precisely, one tracks the spatial evolution of a set of points located on the reference image, which provides a measure of the displacement field and allows the computation of the associated strain field. To each point on index i is associated a correlation domain D . After deformation, one identifies the most similar domains, homologous to the ones of the reference image, by minimizing a correlation function C of null value for perfect similarity. The similarity of a domain D and its transform $\phi(D)$ can be measured by the ‘zero centered normalized cross-correlation coefficient’ C , expressed as:

$$C(\phi_0) = 1 - \frac{\sum_{i \in D} (f(X_i) - \bar{f}_D) \cdot (g(x_i) - \bar{g}_D)}{\sqrt{\sum_{i \in D} (f(X_i) - \bar{f}_D)^2} \cdot \sqrt{\sum_{i \in D} (g(x_i) - \bar{g}_D)^2}}, \quad (1)$$

where X_i and x_i are respectively the coordinates (in pixels) of homologous points in the reference image and in the deformed image, which are associated by an unknown mechanical transformation ϕ , whose ϕ_0 is an approximation, minimizing C ; $f(X)$ and $g(x)$ are respectively the grey levels of point i in the reference image and in the deformed image; \bar{f}_D and \bar{g}_D are respectively the averages of the grey levels on the domain D and on the homologous domain transformed by ϕ_0 . C varies from 0 for perfect match, to a maximum of 2, when fluctuations of f and g are opposite, the value 1 corresponding to no match at all. This measure of similarity is insensitive to a global contrast or brightness variation on the domain between both configurations. The transformation ϕ is assumed to be a translation coupled to a rotation and to a homogeneous deformation, whose gradient is considered equal to the macroscopic gradient. The minimisation of C and an optimisation by bilinear interpolation of the grey levels on each domain D of the deformed image, are realized by the software CorrelManuV from LMS (Bornert, 1996); these two steps allow to determine the displacements with sub-pixel resolution. The coordinates of the centres of the homologous domains determine the displacement field, which is used to calculate the strain field; the latter is obtained on each point of the grid by the average of the transformation gradients affecting a domain delimited by the neighbouring points; the average is obtained by a contour integration on the considered domain (Allais, 1994, Bornert, 1996, Doumalain, 2000). While this method allows the determination of the deformation field only in the observation plane, the out of plane component, can however be evaluated by assuming an axisymmetric deformation and a constant strain in the third direction.

The deformation field is represented by a deformation map superimposed on the microstructure images. At each point of the grid, the component of the deformation is symbolized by a cross of colour function of its value in the neighbourhood of the point. The equivalent deformation of Von Mises ϵ_{eq} , characterising the distortion in the plane and corresponding to the quadratic norm of the deviatoric part of the strain, is:

$$\varepsilon_{eq} = \frac{2}{3} \sqrt{(\varepsilon_{11} - \varepsilon_{22})^2 + 4(\varepsilon_{12})^2} . (2)$$

EXPERIMENTAL OPTICAL AND SEM COMPRESSION SET UPS

Optical / Compression Set-Up and Sample Preparation

The macroscopic compression tests are performed on a uniaxial loading system driven in displacement by means of LVDT sensors. The cylindrical samples are initially of 100mm height and 50mm diameter. The applied load is measured by a force sensor placed on the upper piston. The displacement rate is imposed at 1 μ m/s ($\varepsilon_a \sim 10^{-6} \text{s}^{-1}$). The loading is applied up to sample failure for $\sigma_a \sim 15 \text{MPa}$ of axial stress and less than $\varepsilon_a \sim 0.5\%$ of axial strain, for an experimental duration of $\sim 10 \text{min}$. During this time, up to 250 images are captured at constant time intervals, at the two scales of observation, on two opposite sides of the sample, on which flat surfaces have been machined. On one side, a CCD camera Imperx (4872x3248 $\sim 16 \text{Mpixel}$) covers integrally the sample with pixel size $\sim 22 \mu\text{m}$; on the opposite side, a CCD Spot camera (2048x2048 $\sim 4 \text{Mpixel}$) covers a restricted zone of 7,5mm side with pixel size $\sim 3,5 \mu\text{m}$. Stippled patterns spread on this surface with a painting spray, are used to enhance the local contrasts and to define the reference points. Those paint patches need to be smaller than the measurement basis and their sizes vary here between 10 and 100 μ m to cover few pixels. The axes of both cameras are carefully aligned perpendicularly to the surfaces. The lightings of the sample surfaces need to furnish the wider grey level histogram, with no saturation. The camera Imperx uses a direct lightning by an annular halogen, while the Spot camera uses two lateral lamps. The different equipments of the experimental set-up or the loading frame by itself can experience interfering displacements during compression. In order to quantify these induced errors on DIC, before the loading, few images of the sample are recorded after imposing small displacements of the camera platens, first in the observation plane and then along its normal. For the selected operation conditions, the errors on displacement measurements were quantified respectively at 0,03% and 0,04% for the macroscopic and mesoscopic correlations.

SEM / Compression Set-Up and Sample Preparation

The chamber of the FEI Environmental Scanning Electron Microscope (ESEM) Quanta 600 has been equipped with a miniaturized simple compression system, driven in displacement as well, with a rate of $\sim 1 \mu\text{m/s}$ ($\varepsilon_a \sim 10^{-4} \text{s}^{-1}$). Here, the loading is realized on small parallelepiped samples (height $\sim 20 \text{mm}$, side $\sim 10 \text{mm}$) in a step wise manner (Fig.7); since the SEM acquisition times need several minutes, at most, five increments can be reasonably performed during one single test. The natural contrast between the different components of the material of SEM in Secondary Electron (SE) mode is sufficient for DIC. Contrast and brightness are adjusted before each acquisition in such way that the grey level histograms cover most of the 256 levels (8bits) with no saturation. The size of the high energy electron beam and the scanning rate (raster like – either 30 μ s or 15 μ s, corresponding respectively to acquisition time of 7 and 3.5 min) are adjusted to obtain the good compromise between the signal/noise ratio and the problems of charge accumulation. The magnification x40 covers about a quarter of the sample, i.e. $\sim 3.5 \text{mm}^2$ with a resolution of $\sim 1 \mu\text{m/pix}$; this scale gives some information on local phenomena, but still remains representative of the whole sample. The magnification x160 allows a resolution up to $\sim 250 \text{nm/pix}$. The samples loading faces are rectified by polishing to insure a good distribution of the load. The observation surface is also polished, coated with gold and grounded to allow evacuation of accumulated static

charges. Images, at the initial state and for two imposed displacements of the platens were captured as well to estimate the error on displacement measurements, of 0.13%.

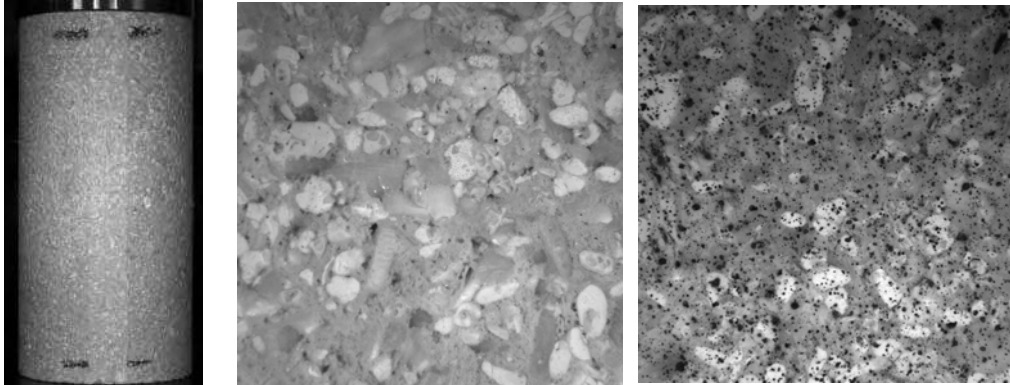


Figure 3: Optical images of Estailades samples; (left) macroscopic full view; (center) mesoscopic spot view; (right) application of speckle painting patterns.

RESULTS OF DIC – MACROSCOPIC TEST IN OPTIC Macroscopic DIC

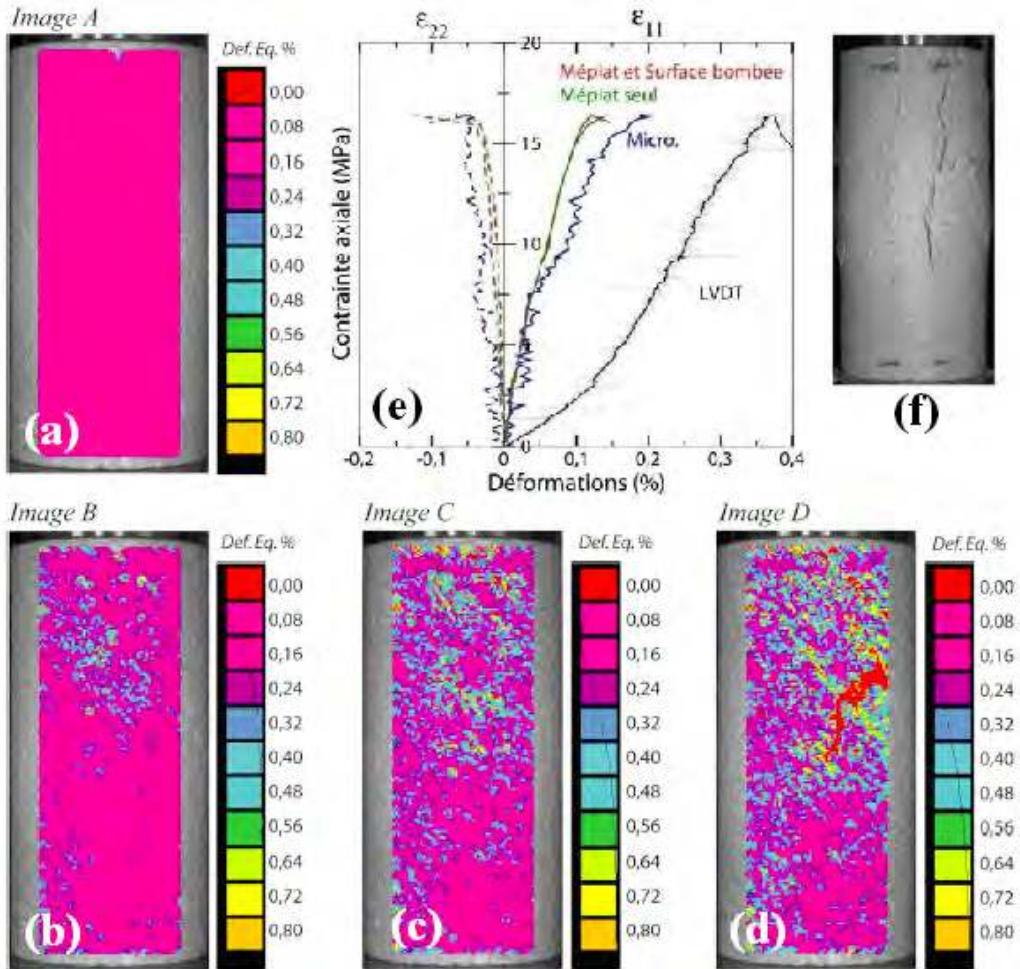


Figure 4: Equivalent deformation maps superimposed on images of Full View camera of sample EST_OPT_A at four levels of continuous loading ((a) $\epsilon_A=0.10\%$, (b) $\epsilon_B=0.20\%$, (c) $\epsilon_C=0.30\%$ and (d) $\epsilon_D=0.37\%$) measured by LVDT (e), up to brittle failure (f). Compression acts vertically.

Figure 4(e) presents the macroscopic loading curve of sample EST_OPT_A, with global axial strain measured by LVDT as a function of the applied stress. The Young modulus calculated through this experimental stress-strain curve is $\sim 6\text{GPa}$. The brittle failure of the sample is obtained for $\epsilon_a \sim 0.37\%$ at a peak stress of $\sim 16\text{MPa}$. Figures 4(a,b,c,d) present the deformation maps calculated at four levels of loading, superimposed on the sample images. The colour is associated to the intensity of ϵ_{eq} . During the initial loading phase of the sample (setting up, initial hardening), up to $\epsilon_A \sim 0.1\%$ (Fig.4(a)), the strain field remains homogeneous. A deformation lens starts to appear when the axial strain reaches $\epsilon_B \sim 0.2\%$ (Fig.4(b)), it later develops and generates a deformation gradient along the sample which is well established for the axial strain $\epsilon_C \sim 0.3\%$ (Fig.4(c)). At this point; the local equivalent strains computed in the upper part of the sample are about ten times larger than in the lower part. Just before the peak stress, at $\epsilon_D \sim 0.37\%$ (Fig.4(d)), at the onset of dilatancy, a strong deformation localization is revealed by DIC, and it announces the site of the macroscopic fracture. The axial equivalent strain as computed by DIC in the neighbourhood of the macroscopic fracture propagation is three times higher than in the lower part of the sample. This has to be correlated to microstructural analysis along the sample length, which shows a higher concentration of clusters of dense aggregates in the central zone of the sample, where the fracture propagates, whereas in the lower part, a more homogeneous repartition of dense and micro-porous aggregates is observed. If we consider now the axial and radial strains computed by DIC, we check that the results of measures at the macroscopic and the mesoscopic scales are consistent, but that later are quite noisier. The deformations obtained by DIC on the flat surface only and on a larger domain (covering the lateral curvature) are identical because the camera depth of field covers most of the sample. The DIC macroscopic measurement yields a Young Modulus of $\sim 13\text{GPa}$ and a Poisson ratio of ~ 0.25 , much larger than the value obtained with the LVDT sensor; the source of the discrepancy is that the LVDT records the initial setup of the sample and deformations of the testing device which is not perfectly rigid.

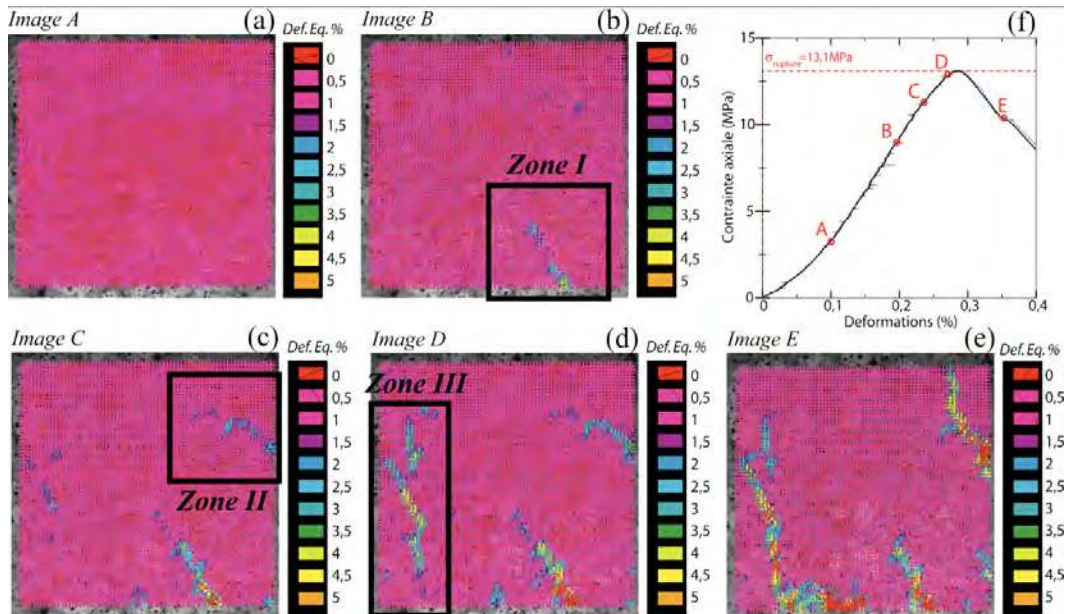


Figure 5: Equivalent deformation maps superimposed on images of Spot camera of sample EST_OPT_B at five levels of continuous loading ((a) $\epsilon_A=0.10\%$, (b) $\epsilon_B=0.20\%$, (c) $\epsilon_C=0.23\%$, (d) $\epsilon_D=0.26\%$ and (e) $\epsilon_E=0.35\%$) measured by LVDT (f). Compression acts vertically.

Mesoscopic DIC

The region observed at a mesoscopic scale is shown in Fig.3(center). This particular choice was guided by the heterogeneities which are present in this area. Indeed, the lower and upper parts of this zone present different concentrations of dense aggregates, while the central part is composed almost exclusively of microporous aggregates. Figure 5 presents the macroscopic loading curve of sample EST_OPT_B and five images labelled A to E showing the deformation maps calculated at the five respective levels of loading shown on the loading curve, superimposed on the picture of the surface of the sample. As it has been observed macroscopically, the deformation field is homogeneous during the initial loading, up to $\epsilon_A \sim 0.1\%$ (Fig.5, Image A) and the studied region does not show any localization, despite the structural heterogeneities. For equivalent strains larger than $\epsilon_B \sim 0.2\%$, different events of localization appear successively in weaker zones, corresponding to the opening of interaggregate porosity (mesoporosity) with the same orientation with respect to the loading direction and relative movement of surrounding aggregates (Fig.5, Images B and C). These microcracks propagate around both denser and microporous aggregates gathered at centre of the zone (Fig.5, Image D), and reach a maximum density just before the peak stress at $\epsilon_A \sim 0.3\%$ (Fig.5, Image D). A strong relaxation associated to the coalescence of the microcracks through the denser aggregates follows the macroscopic failure (Fig.5, Image E).

RESULTS OF DIC – MICROSCOPIC TESTS IN SEM

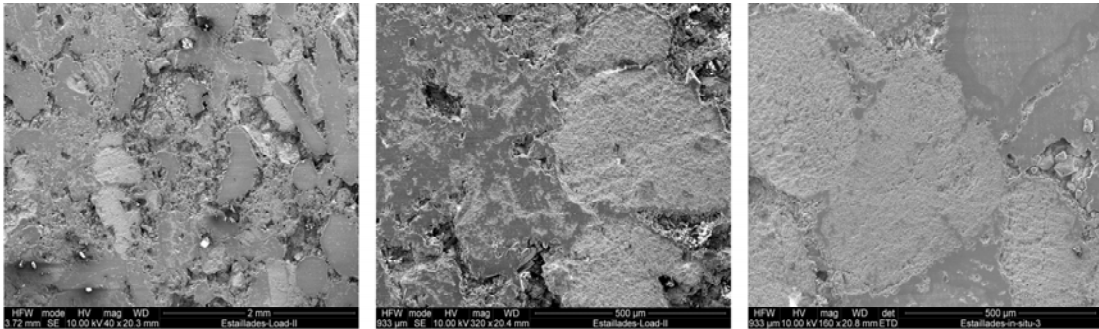


Figure 6: Selected SEM zones of observation on two different samples for DIC; (left and center) position 5 (magnification x40) and 9 (x160) of the first experiment (sample EST_MEB_A); (right) position 6 (magnification x160) of the second experiment (sample EST_MEB_B).

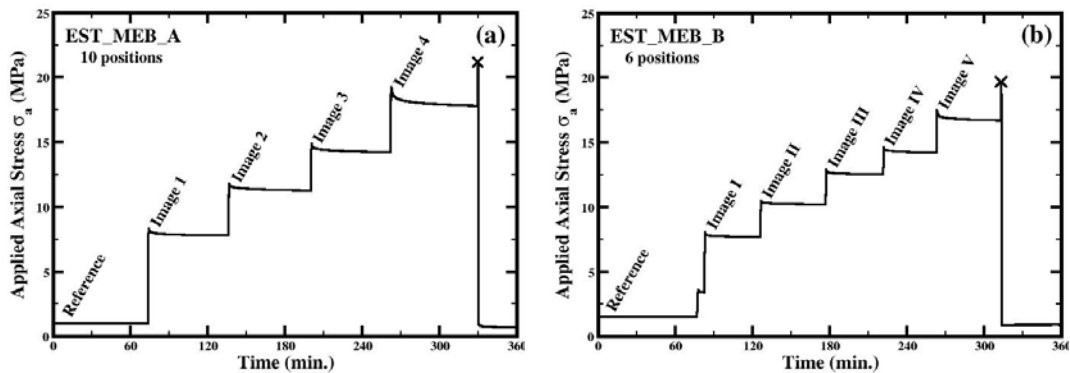


Figure 7: Loading history of samples (a) EST_MEB_A and (b) EST_MEB_B. 4 and 5 loading increments were respectively applied, up to sample failure close to 20MPa. Before acquisition, the sample is allowed to relax stresses; then 10 and 6 zones respectively were imaged at each step but only 3 are presented here; each experiment lasts for approximately 5 hours.

The objective of the microscopic approach is to detect the local deformation mechanisms activated at the scale of the microstructure, during the incremental loading (Fig. 7(a, b)), which will impact the deformations at larger scales.

First Sample – Position 5 and 9

The size of the studied region, $\sim 2.5 \times 2 \text{ mm}^2$ (Fig.6(a)), is comparable to the optical mesoscopic scale, but the image resolution is far better which allows a detailed observation of the different aggregates (Fig.6(b,c)). Figure 8 shows the equivalent deformation maps calculated on images acquired at three consecutive loading steps $\epsilon_2 \sim 0.25\%$, $\epsilon_3 \sim 0.35\%$ and $\epsilon_4 \sim 0.5\%$ (see Fig.7(a)). These maps (Fig. 8, Images 2, 3 and 4) clearly show the progressive evolution of a localization of the deformation, which appear at early compression level. This localization appears at the interfaces of dense aggregates (dark grey), corresponding to zones of large porosity. The localization mechanism is itself essentially the opening of a microcrack at the centre of the region, whose tortuous propagation is conditioned by the arrangement of the aggregates. While, few other localization events, of lower amplitude, appear at the interfaces of dense aggregates on the bottom left part of the image (Fig.8, Image 4) close to the peak stress, no localization is observed inside the microporous aggregates (light grey). Using DIC, we highlight that the propagation of microcracks is not instantaneous, but rather gradual along the regions of weaker strength; we also observe that local displacements are much larger along the more tortuous pathway of the microcracks. At the last loading step (Fig.7(a)), the sample undergoes a stress relaxation of $\sim 3 \text{ MPa}$ which is larger than for the previous steps. This strong relaxation is associated to a large opening of cracks in the central zone, where the local strains exceed 10%, corresponding to a relative displacement of the crack lips of approximately 6 pixels, and which initiates the branching of the principal crack. At this scale, this branching seems not to propagate inside the encountered microporous aggregate (hexagonal region in Fig.8, Image 4), while another crack is opening on the other side.

The microporous and generally homogeneous structure of these aggregates are very likely the factors, which help to accommodate the deformation in a diffuse manner. Consequently, this structure contributes to maintain the integrity of the sample during compression. However, if there are some pre-existing inhomogeneities or microdefects, localization may appear as shown in Figure 9 at the scale of a few aggregates using magnification $\times 160$; the considered region (Fig. 9, Image 4), of size $\sim 0.75 \times 0.5 \text{ mm}^2$, is constituted of microporous aggregates on the right side and dense aggregates on the left side, with ill-defined contours. The strongest localisation in this region is observed by cracking in the more porous zone at the interfaces between the different kinds of aggregates (Fig.9, Image 2), but a compactant localization appears also inside the large microporous aggregate, containing an island of higher porosity (Fig.9, Image 3). These local pre-existing damaged zones inside the microporous aggregates are common; their closure takes place only when they are oriented perpendicularly to the loading direction.

Second Sample – Position 6

The considered region (Fig. 6(c)), of size $\sim 0.75 \times 0.5 \text{ mm}^2$, is constituted of few microporous aggregates, with a large central grain showing a tenuous crossing crack, in contact with a dense aggregate showing a wide crack. At early loading, $\epsilon_2 \sim 0.25\%$, in zone [1] a first compactant localisation appears at the interface of three microporous aggregates, perpendicularly to the direction of compression. At higher compression,

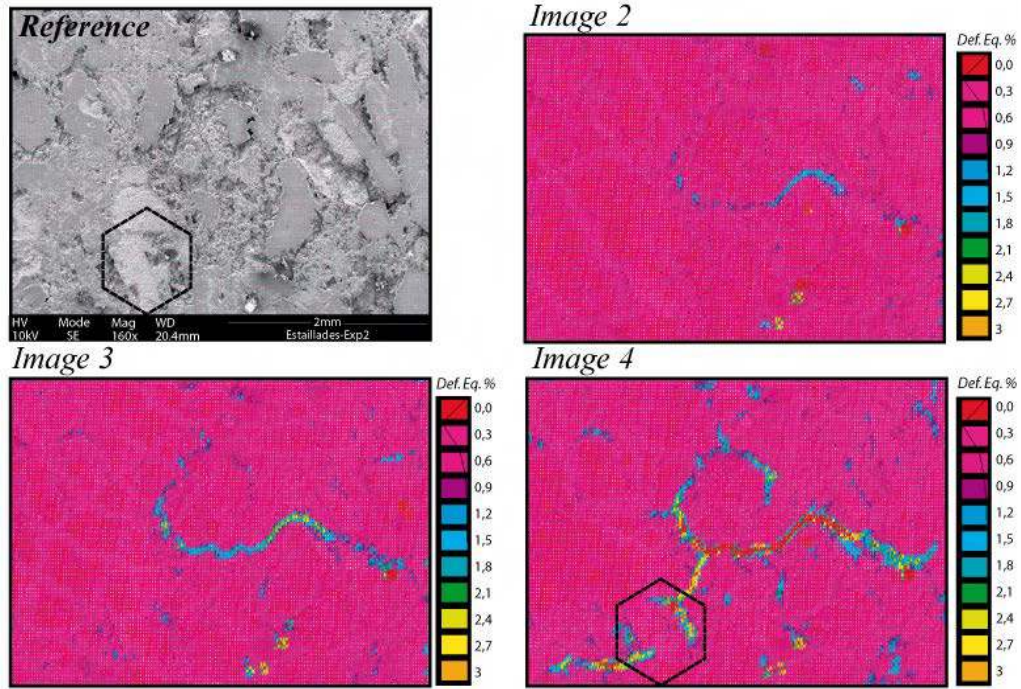


Figure 8: Equivalent deformation maps superimposed on SEM image of sample EST_MEB_A acquired at magnification x40 at three consecutive steps of loading (out of four) $\epsilon_2 \sim 0.25\%$, $\epsilon_3 \sim 0.35\%$ and $\epsilon_4 \sim 0.5\%$. Compression acts horizontally.

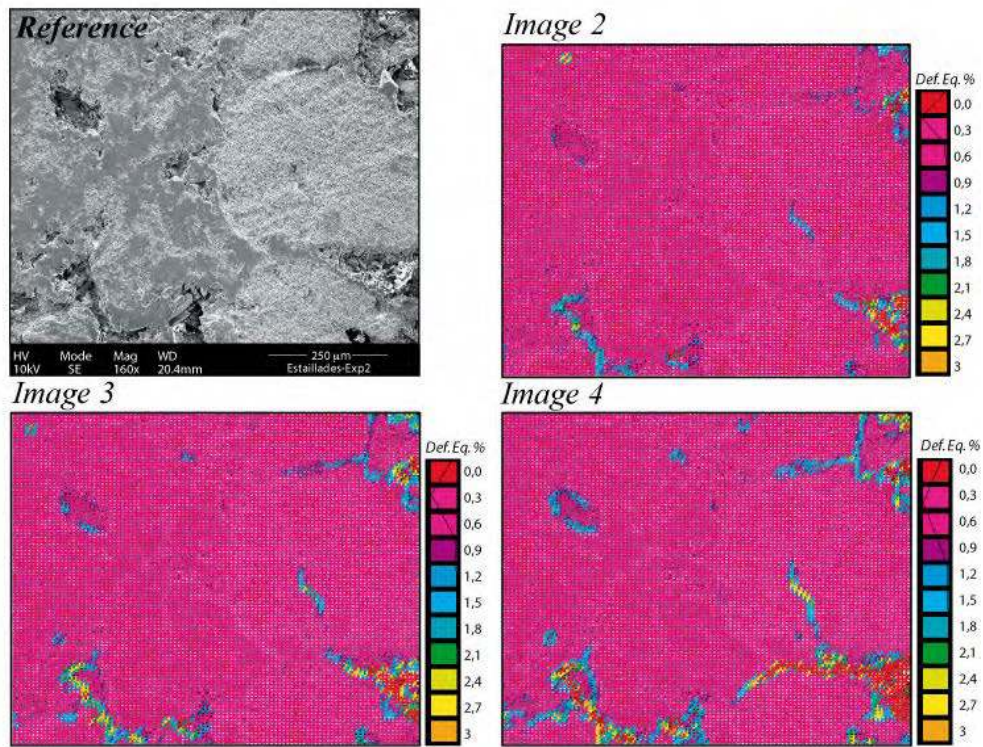


Figure 9: Equivalent deformation maps superimposed on SEM image of sample EST_MEB_A acquired at magnification x160 at three consecutive steps of loading (out of four) $\epsilon_2 \sim 0.25\%$, $\epsilon_3 \sim 0.35\%$ and $\epsilon_4 \sim 0.5\%$. Compression acts horizontally.

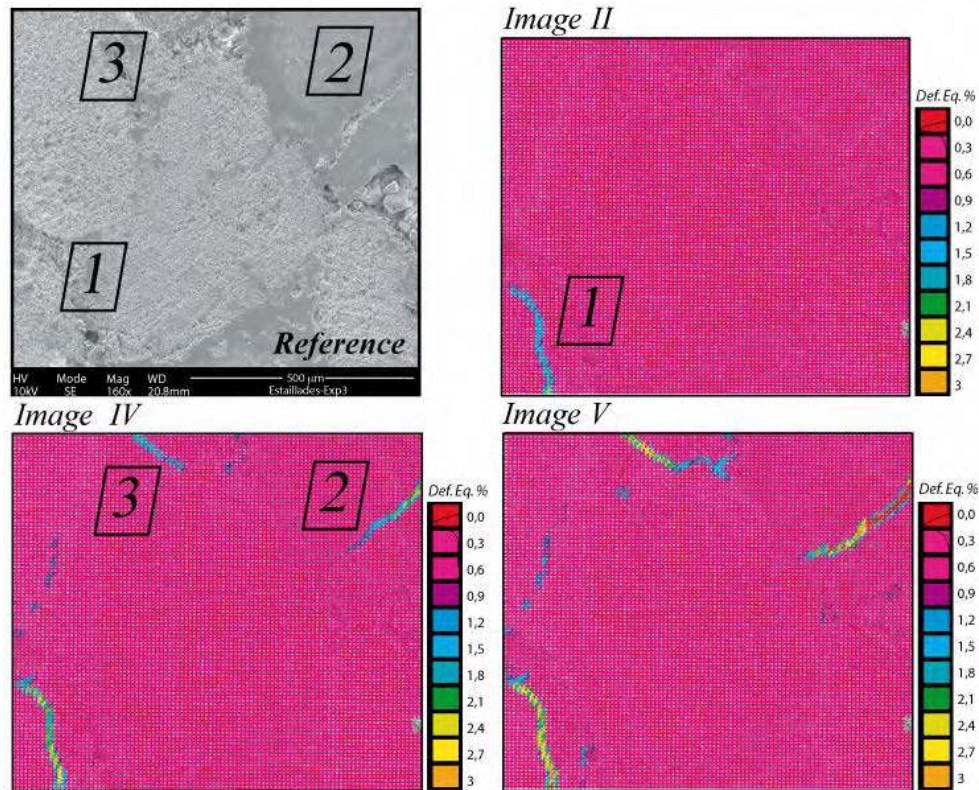


Figure 10: Equivalent deformation maps superimposed on SEM image of sample EST_MEB_B acquired at magnification $\times 40$ at three consecutive steps of loading (out of five) $\varepsilon_{II} \sim 0.25\%$, $\varepsilon_{IV} \sim 0.5\%$ and $\varepsilon_V \sim 0.75\%$. Compression acts horizontally.

$\varepsilon_4 \sim 0.5\%$, simultaneously, in zone [2] the weak zone in the dense aggregates is activated and opening and in zone [3] the microporous aggregates begin to slide at their interfaces. All along the loading, the central microporous aggregate, in spite of its thin crossing microcrack, does not show any sign of localization and seems to accommodate the deformation in a diffuse manner.

CONCLUSIONS

We have tested and applied the 2D image correlation method to a heterogeneous carbonate submitted to compression. Because the level of deformation at yield is very small, it was crucial to quantify rigorously the errors associated to the method. An important stage of image quality optimisation by improvement of local contrast and choice of adapted correlation parameters (grid size, size of correlation domains) was carried out in order to obtain a satisfactory compromise between precise computation of the displacement and strain fields and precision on the extent of the localization. The complementarity of the different scales of observation allows to assess the different modes of deformation and to understand the sequence of their appearance and activity during a loading cycle. At both scales of observation on the macroscopic samples, the treatment of the images acquired during loading yield consistent results and gives a correct estimate of the amounts of global deformations. DIC allows to characterize the impact of mesoscopic heterogeneities on the early warning signs of localisation of the deformation, but also to observe the early apparition of an important microcrack network. This method also shows that strain measurements by conventional gages are

not precise enough. At the SEM scales, the field measurement reveals deformation micromechanisms not visible by simple observation of the images. It confirms the assumption of diffuse accommodation of the deformation in the microporous aggregates and the opening of cracks at the interfaces and in the porous zones. Obviously, the representativity of results obtained from 2D observations on a surface are questionable; in order to bring new elements to this debate, 3D DIC coupled with Micro-Tomography and in-situ compression would be required, but for now, it can only be done at the cost of a downgraded spatial resolution. For now, while DIC clearly highlights the role of heterogeneities on strains distribution and damage propagation towards localization, the step consisting in performing the hydromechanical micro-macro transition is still to come by combining 3D DIC and Micro-Tomography techniques while performing in-situ triaxial compression tests and flow experiments. This approach will require a micro triaxial flow cell, operating in saturated drained condition, to impose triaxial conditions more representative of a reservoir stress state and to link directly the evolutions of permeability to strains.

ACKNOWLEDGEMENTS

At LMS, we are grateful to D. Caldemaison and P. Vally for technical assistance with the SEM apparatus and the testing machine respectively. At IFP, we thank E. Bemmerl, J. Guelard and V. Poitribeau for the petrophysical and dry mechanical characterizations.

REFERENCES

- Allais L., Bornert M., Bretheau T. and Caldemaison D., 'Experimental characterisation of the local strain field in a heterogeneous elastoplastic material', *Acta Metall. Mater.*, **42**, 1994.
- Bornert M., 'Morphologie microstructurale et comportement mécanique', *Thesis EDX*, 1996.
- Bruck H.A., McNeill S.R., Sutton M.A. and Peters W.H., 'DIC using Newton-Raphson method of partial differential correction', *Experimental Mech.*, **29**(3), 1989.
- Chu T., Ranson W., Sutton M. and Peters W., 'Applications of DIC techniques to experimental mechanics', *Experimental Mech.*, **25**, 1985.
- Crawford B.R. and Yale D.P., 'Constitutive Modelling of Deformation and Permeability: Relationships between Critical State and Micromechanics', *SPE/ISRM*, **78189**, 1-10, 2002.
- Dautriat J., 'Comportement hydromécanique des roches réservoirs', *Thesis EDX*, 2009.
- Dautriat J., Gland N., Youssef S., Rosenberg E. and Bekri S., 'Stress-Dependent Directional Permeabilities of Two Analog Reservoir Rocks: A Prospective Study on Contribution of μ -Tomography and Pore Network Models', *SPE Reserv. Eval. & Eng.*, **12**(2), 2009.
- Dautriat J., Gland N., Dimanov A., Raphanel J and Vizika O., 'Laboratory determination of stress-path dependency of directional permeabilities of Estailades Limestone', *SCA* **26**, 2008.
- Doumalin P., 'Microextensométrie par corrélation d'images', *Thesis Ecole Polytechnique*, 2000.
- Doumalin P., Bornert M. and Caldemaison D., 'Microextensometry by DIC applied to micromechanical studies using SEM', *Proc. Int. Conf. Adv. Techn. Exp. Mech.*, 1999.
- LeNoir N., Bornert M., Desrues J., Besuelle P. and Viggiani G., 'Volumetric DIC applied to RX μ -tomography images from triaxial compression tests on argillaceous rock', *Strain*, **43**(3), 2007.
- Schutjens P. and De Ruig H., 'The Influence of Stress Path on Compressibility and Permeability of an Overpressurized Reservoir', *Phys. Chem. Earth (A)*, **22**, 97-103, 1997.
- Valès F., 'Modes de déformation et d'endommagement de roches argileuses', *Thesis EDX*, 2008.
- Valès F., Bornert M., Gharbi H., Nguyen Minh D. and Eytard J.C., 'Micromechanical Investigations of the hydro-mechanical behaviour of argillite rocks, by means of optical full field strain measurement and acoustic emission techniques', *Proc. Int. Soc. Rock Mech.*, 2007.
- Yale D.P. and Crawford B., "Plasticity and Permeability in Carbonates: Dependence on Stress Path and Porosity", *SPE/ISRM*, **47582**, 485-494, 1998.